


Selectable diffusion direction with topologically protected edge modes

Keita Funayama ¹✉, Jun Hirotsu², Atsushi Miura¹ & Hiroya Tanaka¹

Topological insulators provide great potential to control diffusion phenomena as well as waves. In addition to the thermal localization and robust decay as reported, the topological edge states with higher degree of freedom offers a route to control directional diffusion. Here, we show that the direction of thermal diffusion can be selected by the contributions of the topologically protected edge modes in a honeycomb-shaped structure. Considering the thermal diffusion between the nearest neighboring sites of the honeycomb-shaped unit cells, the cells allow unidirectional heat balance from a macroscopic perspective when we set the structure to the temperature corresponding to the edge mode type. Moreover, this diffusion system is found to be immune to defects owing to the robustness of topological states. Our work points to exciting avenues for controlling diffusion phenomena.

¹Toyota Central R&D Labs., Inc., Nagakute 480-1192, Japan. ²Department of Micro Engineering, Kyoto University, Kyoto 615-8540, Japan.
✉email: funayama@mosk.tytlabs.co.jp

There is now significant interest in exploiting topological properties in a wide variety of physical wave systems such as electromagnetic^{1–6}, acoustic^{7–9}, and mechanical systems^{10–16}. One of the characteristic topological phenomena is the emergence of robust edge modes. The methodology based on the Su–Schrieffer–Heeger (SSH) model is the most common method for the emergence of edge modes^{17,18}. This has allowed wave control with topological insulators in one-dimensional (1D) classical systems^{19–22}. In addition, the quantum spin Hall effect (QSHE) has attracted significant attention owing to its higher degree of freedom than that of the SSH model. The QSHE-based topological states can control wave systems in higher dimensions, thereby enabling localization^{23–25} and one-way wave propagation^{26–29}.

Recent theoretical and experimental studies have demonstrated that topological edge modes can be applied to diffusion systems. Pioneering studies showed that heat distribution localizes in 1D structures with robust thermal decay based on the SSH model^{30–33}. The higher-order topological corner modes expanded the potential of thermal diffusion control in two-dimensional (2D) diffusion systems³⁴. By considering topological diffusion phenomena in 2D structures, other topological models, such as the Kagome lattice, were applied to the diffusion systems³⁵. These investigations revealed the localization of high- or low-temperature spots with topological locking decay rates in 2D diffusion systems. However, these systems controlled only the localization and decay temperature rate and did not realize the more-desired high-dimensional heat-management schemes, such as heat transport and thermal polarization. To achieve topological-based heat transport, recent studies have proposed Hermitian systems based on combined thermal distribution and fluid convection, i.e., the skin effect^{36–38}. These systems have achieved unidirectional heat transport through the edges of the structures. However, higher-dimensional structures (more than 2D) require flow paths that tend to be complicated and are difficult to ensure broad scalability for applications ranging from massive thermal systems to microscale devices. In addition, the topological states with a higher degree of freedom, such as the QSHE, which has immense potential to control diffusion phenomena with a simple diffusivity design, have not been investigated sufficiently in diffusion systems.

In this paper, we demonstrate that QSHE-inspired topologically protected edge modes appear in a thermal diffusion system consisting of honeycomb-shaped unit cells. We consider that the heat transfer in our structure at the topological and ordinary states. From numerical and analytical studies, we show that the temperature corresponding to the edge modes macroscopically provides directional heat balance in the unit cells by considering the thermal diffusion between the neighboring sites. As the result of the temporal evolution of the diffusion for such a temperature distribution, the edge modes induce thermal polarization in the 2D structure. Consequently, the macroscopic diffusion direction can be selected based on the type of excited edge mode. We also verified a well-known unique characteristic of topological edge modes, which is that they are immune to defects. Our results indicate that the use of topological edge modes has the potential to control thermal polarization in any direction. Generally, our work should motivate systematic studies to apply topological properties to all diffusion phenomena.

Results

Design of a topological diffusion system. Our structure consists of periodically aligned honeycomb-shaped unit cells, as illustrated in Fig. 1a. The unit cell has six circle sites. The nearest-

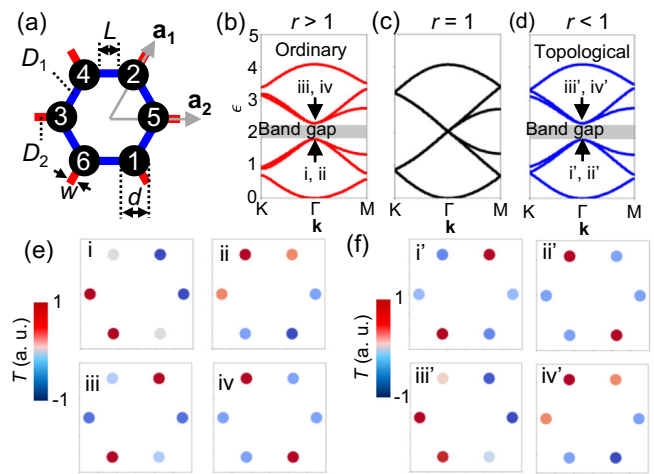


Fig. 1 Unit design for topological and ordinary states. **a** Schematic of the honeycomb-shaped unit cell. Each of the nearest neighboring sites (black) is connected by the beams with the effective diffusivity D_1 (blue). The neighboring unit cells are connected by the beams with the effective diffusivity D_2 (red). D_1 and D_2 are effective diffusivities obtained by normalizing thermal diffusivities ($\lambda c^{-1} \rho^{-1}$) with L^{-2} . λ , c , and ρ are thermal conductivity, thermal capacity, and density, respectively. $L = 15$ mm and $w = 2$ mm are the length and width of the beams. $d = 20$ mm is the diameter of the disc-shaped site. \mathbf{a}_1 and \mathbf{a}_2 are unit vectors. **b–d** Spectra of the eigenvalues for the infinite periodic honeycomb lattice with **(b)** $r > 1$ ($D_1 = 0.765$, $D_2 = 0.518$), **(c)** $r = 1$ ($D_1 = D_2 = 0.68$), and **(d)** $r < 1$ ($D_1 = 0.6$, $D_2 = 0.85$). r is the ratio of D_1 and D_2 . Each of the doubly degenerated modes in **(b)** and **(d)** are labeled as i - iv and i' - iv' . **e, f** Site temperature corresponding to the eigenfunctions in the unit cell at modes **(e)** i - iv and **(f)** i' - iv' .

neighboring sites and unit cells are connected by fine beams with the effective diffusivities D_1 and D_2 . As a result, the equation of thermal diffusion in a unit cell is expressed by the 6×6 effective diffusivity matrix to ensure the parallel periodicity of the structure:

$$\frac{\partial}{\partial t} \begin{bmatrix} T_1 \\ \vdots \\ T_6 \end{bmatrix} = \begin{bmatrix} Q & P_1 \\ P_2 & Q \end{bmatrix} \begin{bmatrix} T_1 \\ \vdots \\ T_6 \end{bmatrix}, \quad (1)$$

where

$$Q = \begin{bmatrix} -(2D_1 + D_2) & 0 & 0 \\ 0 & \ddots & \vdots \\ 0 & \cdots & -(2D_1 + D_2) \end{bmatrix}, \quad (2)$$

$$P_{1(2)} = \begin{bmatrix} D_2 e^{-i\mathbf{k} \cdot (\mathbf{a}_{1(2)} - \mathbf{a}_{2(1)})} & D_1 & D_1 \\ D_1 & D_1 & D_2 e^{i\mathbf{k} \cdot \mathbf{a}_{1(2)}} \\ D_1 & D_2 e^{-i\mathbf{k} \cdot \mathbf{a}_{2(1)}} & D_1 \end{bmatrix}. \quad (3)$$

Here, eigenfunctions, T_1, \dots , and T_6 , denote the temperature at each site as numbered in Fig. 1a, \mathbf{k} is the wavenumber vector, and $\mathbf{a}_{1(2)}$ is the unit vector as shown in Fig. 1a. Note that the wavenumber vector \mathbf{k} expresses the arbitrary position in the first Brillouin zones of the momentum space. The eigenfunction of the Hamiltonian in the momentum space denotes the temperature at the stationary state corresponding to the initial state in the Euclidean space (i.e., $t = 0$).

We design the topological and ordinary unit cells by adjusting the ratio $r = D_1/D_2$ of the two effective diffusivities. The topological phase transition can be controlled via r ^{2,16}.

Diagonalizing the effective diffusivity matrix in Eq. (1), we obtain the spectrum of the eigenvalues ϵ . Figure 1b–d shows the spectra for an infinite periodic honeycomb lattice with $r > 1$, $r = 1$, and $r < 1$. When all the diffusivities in the unit cell have the same value (i.e., $r = 1$), we observe the Dirac cone at the Γ point (Fig. 1c), thus suggesting the existence of a topological surface state. For $r > 1$ and $r < 1$, the spectra have a bandgap and two doubly degenerated modes (Fig. 1b and d).

To identify the state of the structure with $r > 1$ and $r < 1$, we confirm the eigenfunctions of each doubly degenerated mode specified as i–iv in Fig. 1b and i'–iv' in Fig. 1d. The eigenfunctions in these modes correspond to the site temperature in the unit cell. Figure 1e shows the temperature distributions of modes i–iv for $r > 1$. We observe the dipole p_x and p_y modes at modes i and ii, and quadrupole d_{xy} and $d_{x^2-y^2}$ modes at modes iii and iv, respectively. Thus, the lowly and highly polarized modes appear below and above the band gap, respectively. This result indicates that the structure with $r > 1$ is the ordinary state. In contrast, in Fig. 1f, for $r < 1$, modes i' and ii' (iii' and iv') show the quadrupole (dipole) modes. Such an inversion of the order between the dipole and quadrupole modes signifies that the structure with $r < 1$ is the nontrivial topological state.

To demonstrate the topologically protected edge modes in the thermal diffusion system, we consider a supercell with a boundary between the topological and ordinary states, as shown in Fig. 2a. Figure 2b shows the spectra of the supercell. The red and blue lines show the topological edge modes with different polarizations in the unit cells. The gray lines indicate the bulk modes. We focus on the two band-gap-crossing edge modes at $k_x = 0$, which are indicated by the magenta and cyan arrows in Fig. 2b and are specified as modes A and B, respectively.

Figure 2c, d depict the temperature distributions in modes A and B in the supercell. Both temperature distributions are localized around the boundary between topological and ordinary states. The temperatures in modes A and B correspond to the eigenfunction amplitudes obtained by solving the eigenvalue equation, which consists of thermal diffusion equations for all 120 sites in the supercell. Such edge modes have great potential for controlling diffusion phenomena. Indeed, in wave systems, topologically protected edge modes have intriguing characteristics, such as field localization and unidirectional wave propagation^{2,8,11,12,16,24}.

Based on the eigenfunction amplitudes on each site, we analyze heat transfer in modes A and B. Figure 2e, f visualize the diffusion direction and quantity of heat transferred between the sites in the two ordinary and topological unit cells (specified as O2, O1, T1, and T2). The green arrows denote the flow direction, and their widths are the transferred heat quantity between the nearest neighboring sites.

Considering and summing up the local thermal diffusions between each site, we find that the unit cell for modes A and B exhibits a unique directional heat balance. We calculate the heat balances by summing up the heat quantities along the x - and y -axes [right panels in Fig. 2e, f]. In Fig. 2e, the heat balance indicates the thermal flow along the x -axis through the unit cell; there is no heat balance along the y -axis. Thus, mode A apparently rectifies the thermal flow only along the direction parallel to the boundary, i.e., the x -axis. On the other hand, as illustrated in Fig. 2f, mode B provides thermal flow only along the y -axis. Therefore, our structure has the potential to select the direction of macroscopic thermal diffusion based on the local thermal diffusions of the different edge modes.

Edge states and temporal evolution of diffusion. To verify our theoretical prediction for selecting the diffusion direction, we

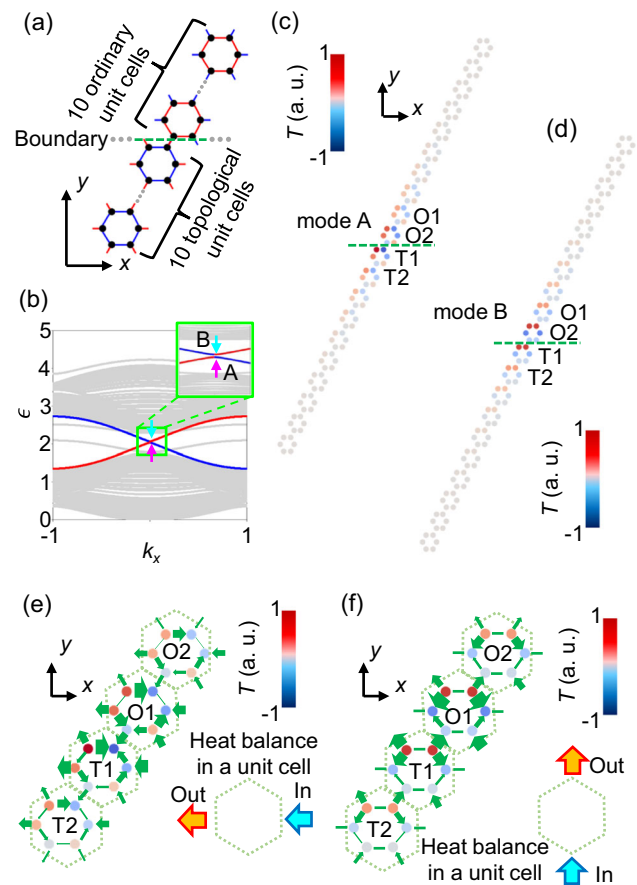


Fig. 2 Spectrum of supercell and temperature distributions for topological edge modes. **a** Schematic of the supercell with a boundary between the topological and ordinary unit cells. The supercell consists of 10 units of topological and ordinary states. **b** Band diagram of the supercell. The blue and red lines denote the topological edge modes. Modes A and B are indicated by magenta and cyan arrows, respectively. The inset shows the enlarged view of the green square. **c, d** Temperature distributions in the supercell at modes **(c)** A and **(d)** B. **e, f** Heat transfer between the sites for the unit cells O2, O1, T1, and T2 at modes **(e)** A and **(f)** B. Green arrows denote the flow direction, and their widths imply the transferred heat quantity between the nearest neighboring sites. Right bottom panels in **e** and **f** show the heat balance in each unit cell.

compute the time evolution of the temperature in modes A and B using COMSOL Multiphysics. Figure 3a shows the model used in the calculation. Each of the half structures in Fig. 3a consists of topological (T) or ordinary (O) states. Details of the simulation settings are described in the “Methods” section. For the numerical investigation, we convert the eigenfunction to temperature $T_{s,v} = T_0 + \alpha T_{s,v}^{A(B)}$ in Kelvin. Here, $T_0 = 293.15$ K is the reference temperature, $\alpha = 100$ is the amplification coefficient, $T_{s,v}^{A(B)}$ is the eigenfunction of mode A (B) at location $\mathbf{v} = [m_x, m_y, n]$ of the n th site ($n \in \{1, \dots, 6\}$) in the m_x th and m_y th cells ($m_x \in \{1, \dots, 13\}$ and $m_y \in \{1, \dots, 6\}$), and $s \in \{O, T\}$ is the ordinary and topological sites. To excite the edge modes to the system, we set the temperature distributions of modes A or B to each site of the unit cells of $m_y = 1$ and $m_y = 2$, which are enclosed by the broken black line in Fig. 3a. The other sites are set to T_0 because the eigenfunction amplitudes are negligibly small in the unit cells of $m_y \geq 3$, owing to the strong localization of the field around the boundary at the edge modes. We indeed observe that the temperature at the site $m_y = 3$ ($T_{s,m_x,3,n}$) is 30% or less of that at the site $m_y = 1$ ($T_{s,m_x,1,n}$), for all m_x and n values.

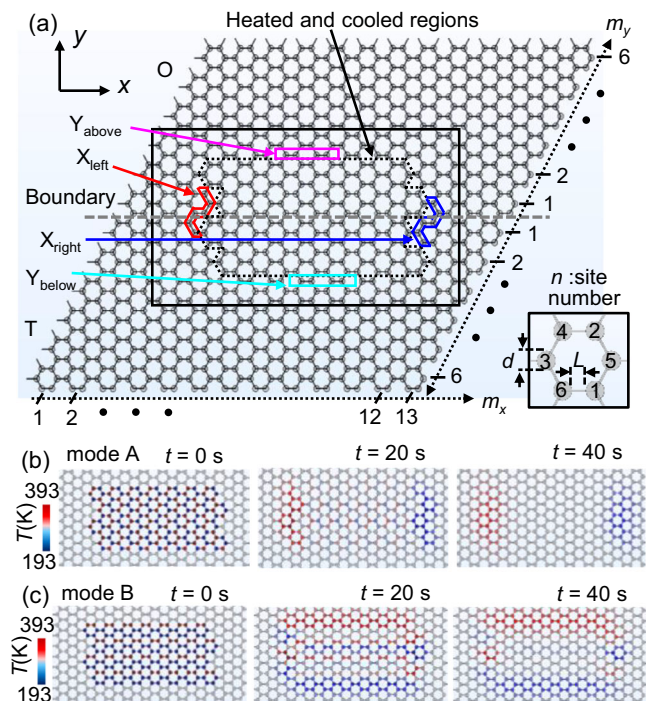


Fig. 3 Simulation results of time-dependent temperature distribution for topological edge modes. **a** Structure with the boundary between the topological and ordinary unit cells. The edge modes are excited in the region enclosed by the broken black line. Initial temperature is $T_0 = 293.15$ K in the area except for the enclosed region. Regions X_{left} (red line), X_{right} (blue line), Y_{above} (magenta line), and Y_{below} (cyan line) are the nearest-neighboring sites from the heated and cooled regions. The thickness of the simulated model is 10 mm, the diameter of the site is $d = 20$ mm, and the distance between the nearest-neighboring sites is the same as the value for the model in Fig. 1 ($L = 15$ mm). **b, c** Snapshots of thermal diffusion at $t = 0, 20$, and 40 s for modes **(b)** A and **(c)** B in the area enclosed by the solid black square in **(a)**.

Figure 3b, c show the numerical time evolution of the temperature distributions for modes A and B in the region enclosed by the solid black square in Fig. 3a. When exciting mode A, we observe high and low temperatures at $t = 40$ s at left and right edges [regions X_{left} and X_{right} in Fig. 3a] (see Fig. 3b). In the topological diffusion system, mode B enables the polarization of the heat distribution along the direction perpendicular to the boundary, unlike the topological wave systems. When exciting mode B, we indeed observe high and low temperatures at above and below edges [regions Y_{above} and Y_{below} in Fig. 3a] (see Fig. 3c). Thus, modes A and B realize macroscopic thermal diffusion only along the x - and y -axis, respectively, as predicted in Fig. 2e, f.

When the symmetry between temperature distributions of the in-phase and antiphase modes coincides with the symmetry of the structure, the eigenequation based on Eq. (1) contains antiphase modes in the eigenvalue solution. Note that the antiphase modes have a counter-rotating temperature distribution in a unit cell to that of in-phase modes. Using the antiphase mode, we can further select the diffusion direction. We now consider the 180° -rotated temperature distribution of mode A about the y -axis as the antiphase mode and refer to it as mode A'. Specifically, temperature distributions of both modes A and A' are axisymmetric about the y -axis. As the supercell also has an axisymmetric structure about the y -axis, the temperature distribution of mode A' can appear as another edge mode.

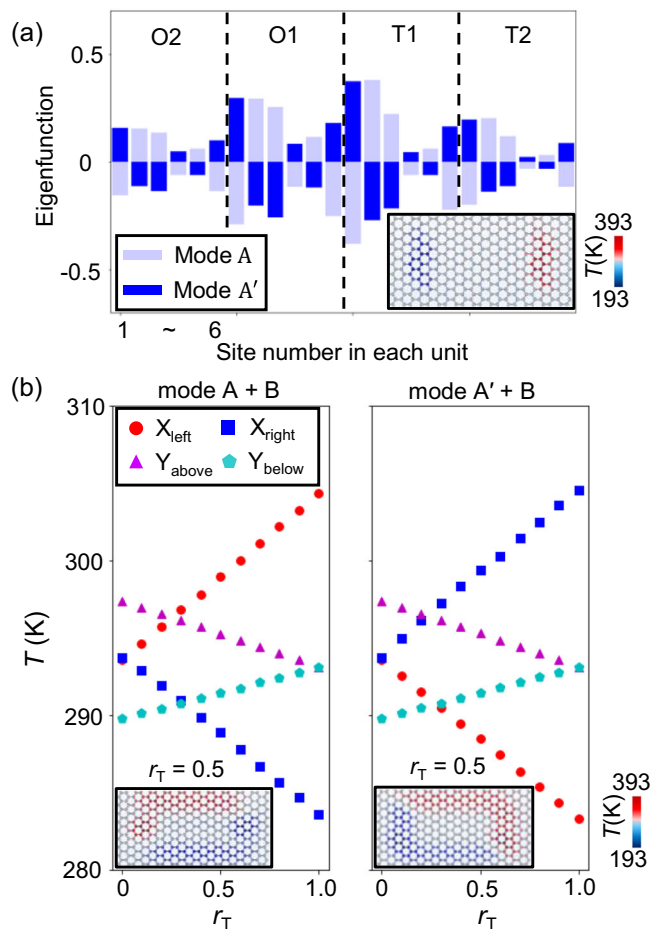


Fig. 4 Results of thermal polarization with in- and anti-phase modes.

a Eigenfunctions of modes A (light blue) and A' (dark blue) on the sites in the unit cells specified as O2, O1, T1, and T2 in Fig. 2. The inset shows the temperature distribution at $t = 40$ s when mode A' is excited to the structure in Fig. 3a. **b** Temperature in regions X_{left} (red), X_{right} (blue), Y_{above} (magenta), and Y_{below} (cyan) at $t = 40$ s as the function of r_T when modes A + B (left) and A' + B (right) are applied to the structure in Fig. 3a. In the calculations for the inset of **(a)** and **(b)**, we use the same simulation settings as that in Fig. 3 except for the initial temperature determined by the applied edge modes. r_T is the ratio of thermal diffusivities D_1 and D_2 in the topological unit cell.

Figure 4a shows the eigenfunctions in cells O1, O2, T1, and T2 of the supercell in mode A (light blue) and A' (dark blue). Mode A' has an eigenvalue at $k_x = 0.02$, as shown by the blue line in Fig. 2b. The eigenfunction of mode A' exhibits an inverted mode A distribution at site O2 (also at sites T1, O2, and T2). Thus, mode A and A' are in opposite phases and this mode property is matched to the symmetry of the structure.

In addition to mode A, we have 180° -rotated mode B around the y -axis as an antiphase mode; we refer to this as mode B'. The temperature distribution in the unit cells for mode B' fully coincides with that for mode B. This axisymmetric property can be readily determined from the distribution in Fig. 2d. As a result, the thermal diffusion resulting from mode B' is equivalent to that of mode B.

Importantly, the inverted initial field about the y -axis affects the thermal polarization. The inset in Fig. 4a shows a snapshot of the temperature distribution at $t = 40$ s when mode A' is excited. High- and low-temperatures are observed in regions X_{right} and X_{left} , respectively. This proves that mode A' inverts the diffusion

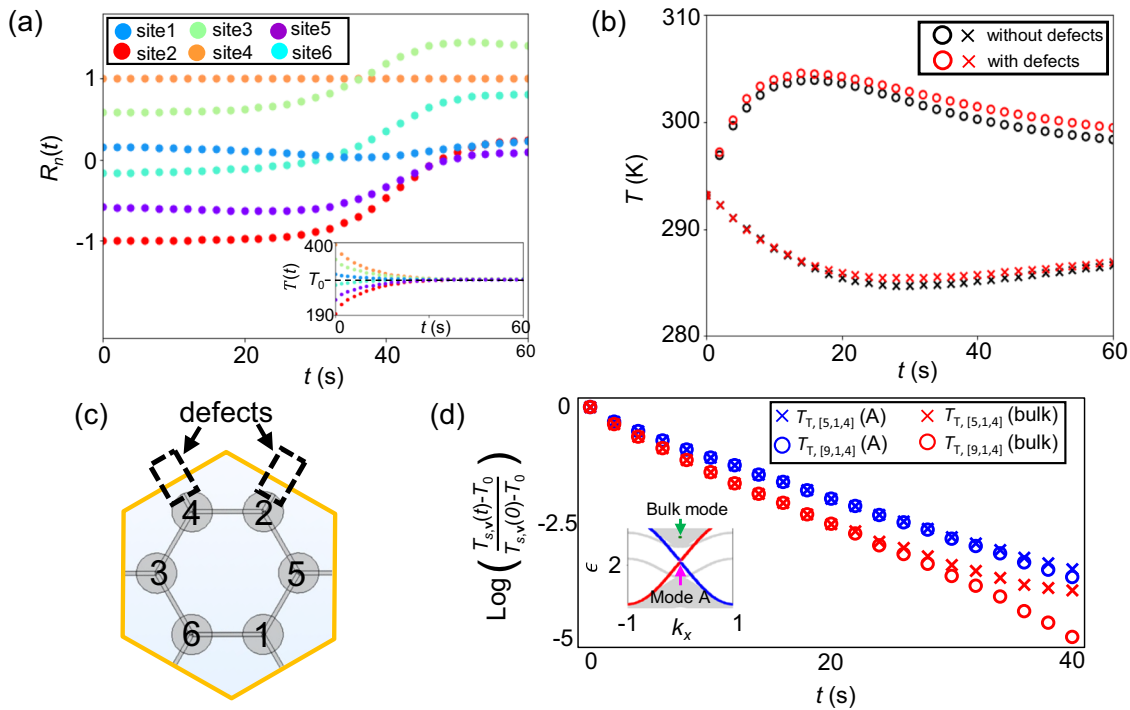


Fig. 5 Immunity to defects. **a** Time dependency of the relative temperature $R_n(t)$ on the six sites in the topological unit cell of $(m_x, m_y) = (7, 1)$ at mode A. The inset shows the temperatures in time on each site. **b** Time dependency of the temperatures in regions X_{left} (circles) and X_{right} (crosses). Red and black symbols show the results with and without the defects, respectively. **c** Schematic of the unit cell including the defects. Sites 2 and 4 lack beams. We use the same simulation settings as that in Fig. 3 except for the defects in (c). **d** Temporal evolutions of normalized temperatures for mode A (blue) and the bulk mode (red). In this case, T_0 is the room temperature ($=293.15$ K). The crosses and circles show the time-dependent temperatures $T_{T,[5,1,4]}$ and $T_{T,[9,1,4]}$. The inset shows the band diagram of the supercell. The magenta and green arrows, respectively, denote mode A and the excited bulk mode.

direction of mode A. However, mode B' does not invert the diffusion direction because of the perfect coincidence of the temperature distribution with B. Thus, we can change the diffusion direction by selecting the initial temperature of the sites based on the three different modes (A, A', and B) in our structure.

Furthermore, our structure enables us to control the diffusion direction owing to the incoherence of the edge modes. Specifically, the mutually incoherent modes A (A') and B can be linearly combined. Using the ratio r_T of modes A (A') and B, we can excite our structure in the combined mode as

$$T_{s,v}^{AB} = r_T T_{s,v}^A + (1 - r_T) T_{s,v}^B, \quad (4)$$

$$T_{s,v}^{A'B} = r_T T_{s,v}^{A'} + (1 - r_T) T_{s,v}^B, \quad (5)$$

where $T_{s,v}^{A'}$ is the eigenfunction of mode A' and $0 \leq r_T \leq 1$. Figure 4b shows the temperature dependence of r_T in regions X_{left} , X_{right} , Y_{above} , and Y_{below} in Fig. 3a at $t = 40$ s. Depending on the type of the combined mode, the temperature in the four regions linearly increases and decreases with an increase in r_T . In particular, when $r_T = 0.5$, we obtain a symmetric temperature distribution about the y -axis (see the insets of Fig. 4b). The results here indicate the potential for designing arbitral temperature distribution and thermal polarization.

Robustness of the edge modes. The edge modes gradually collapse with time after these are applied to the structure. As the unidirectional heat balance of the unit cells continues as long as the edge modes are maintained, the temporal robustness of the edge modes is crucial for designing topological diffusion systems. Focusing on mode A, we evaluate the temperature variation with time for the topological unit cell. Figure 5a shows the relative temperature $R_n(t) = \tilde{T}_{T,n}(t) / \tilde{T}_{T,4}(t)$, considering the unbiased

temperature $\tilde{T}_{T,n}(t) = (T_{T,7,1,n}(t) - T_0) / \alpha$ of the unit cell near the boundary, $(m_x, m_y) = (7, 1)$ in Fig. 3a. For $t < 20$ s, $R_n(t)$ on each site has a constant value, that is, each temperature uniformly decays at the topologically protected decay rate. For $t \geq 20$ s, mode A collapses because the temperatures of the unit cell almost converge to T_0 (see inset of Fig. 5a); thus mode A cannot be maintained. The temporal mode robustness contributes to the duration of the macroscopic directional thermal diffusion. Figure 5b shows the temperatures in regions X_{left} (circles) and X_{right} (crosses) as a function of time. For $t < 20$ s, in region X_{left} (X_{right}), the temperature increases (decreases) with time due to the thermal localization provided by mode A. For $t \geq 20$ s, the temperature in X_{left} (X_{right}) decays (saturates) because the edge mode plays a minor role in the structure.

Finally, we evaluate a unique characteristic of the topologically protected edge modes, which is their immunity to defects. To introduce the defects into our structure, we remove the beams from sites 2 and 4 (see Fig. 5c), for two unit cells $(s, m_x, m_y) = (T, 6, 1)$ and $(T, 8, 1)$. The time dependence of the temperature in regions X_{left} and X_{right} is plotted with red symbols in Fig. 5b. We observe small variations in the temperatures with and without defects. Hence, the edge states are robust against disorders due to topological protection as well as other topological systems.

We compare the thermal decay between the two separate unit cells at mode A and a bulk mode. Mode A exhibits a topological edge mode, whereas the bulk mode exhibits conventional diffusion phenomena. We perform simulations for the model with the defect, which is illustrated in Figs. 3a and 5c. The decay rates, $\gamma_{s,v}$, are then calculated based on the temperature gradient, i.e., $\gamma_{s,v} = -\frac{d}{dt} \log[(T_{s,v}(t) - T_0) / (T_{s,v}(0) - T_0)]$. Figure 5d shows the temperature decay. The blue (red) cross and circle symbols show the temperatures $T_{T,v}$ of $v = [5, 1, 4]$ and $v = [9, 1, 4]$ for

mode A (bulk mode), respectively. The bulk mode is denoted by a green circle in the inset of Fig. 5d. For mode A, the decay rates are $\gamma_{T,[5,1,4]} = 0.0858$ and $\gamma_{T,[9,1,4]} = 0.0891$ with an observed difference of only 3.8%. For the bulk mode, the decay rates are $\gamma_{T,[5,1,4]} = 0.0995$ and $\gamma_{T,[9,1,4]} = 0.1182$ with a difference of 18.8%, which is 4.9 times larger than the value for mode A. Thus, we conclude that the edge modes (instead of the bulk mode) can maintain uniform and robust thermal diffusion due to topological protection despite the existence of defects.

Discussion

We have shown that topologically protected edge modes appear in the diffusion system consisting of the honeycomb-shaped structure, which we have chosen motivated by the QSHE. While previous topological edge modes in diffusion systems could only design the decay rate^{30–32}, the edge states in our structure realize that the diffusion direction is selected based on the type of edge modes. In addition, it is found that the edge modes are immune to defects. The robust modes stably lead to thermal polarization resulting from the unidirectional heat balance of unit cells in realistic diffusion systems. The topological diffusion systems provide a fruitful avenue for temperature control and thermal management. In addition, the selectivity of diffusion direction provided in this paper has a great potential to control other diffusion phenomena.

Note that in the diffusion system consisting of the infinite periodic honeycomb structure, the effective Hamiltonian has a similar configuration to that used in the wave system. Given the similarity of the governing equations between wave and diffusion systems, we should observe the topological edge modes in the diffusion system. To obtain a clear understanding of the analogy between the wave and diffusion systems, we analyze the Fourier components, which are commonly used to study topological materials. It is interesting to note that as the diffusivities are real numbers, the Hamiltonian in our system is expressed as an Anti-Hermitian matrix, which is a distinctly different point from the wave system. This anti-Hermitian matrix provides the imaginary eigenvalues, thereby denoting the edge modes with a topologically protected decay rate. Thus, the edge modes in our structure are characterized in terms of nonstationary temperature decay. To clarify the temporal response of our system, we studied the temperature decay based on numerical simulations.

The diffusion phenomena restrict the topological protection within a finite time. We should design the possible topologically protected duration by tuning the decay rate. When the decay rate is low, the edge modes are maintained for a long time due to the slow response time of the system. By contrast, high decay rates lead to fast thermal diffusion processes, resulting in the fast destruction of the edge mode. Therefore, we should consider a trade-off between the topologically protected duration and the response time to meet the application requirements.

We require an adequate number of supercells in the x -axis to maintain the edge modes. The unit cells in contact with the edges of the sample device [e.g., $m_x = 4$ and 10 when $m_y = 1$ and $s = T$ in the structure of Fig. 3a] cannot maintain the one-directional heat balance. This is because the periodicity of the cell is eliminated; therefore, it is not possible to obtain the inflow and outflow heat that the edge mode guarantees. Hence, we require at least one supercell structure flanked by two edge supercells. In other words, the system should have three supercells to maintain uniform directional diffusion.

Again, our approach taken here exploits the topological edge modes in the honeycomb structure for the selectable direction of

the macroscopic thermal diffusion that results in thermal polarization. This can potentially be extended to other diffusion phenomena, e.g., ion transport. An interesting point is that ionic transport is described by internal and external factors unlike thermal diffusion. Specifically, ionic diffusivity is affected by external factors (e.g., ambient temperature) as well as internal material properties such as number of the mobile ions, charge, and activation energy. The ambient temperature can be adjusted by applying external signals. Hence, it will be possible to actively control the topological and ordinary states via the ambient temperature in ion transport systems. Design for topological systems depending on both internal and external factors is a crucial future work.

In the QSHE edge modes are helical and exhibit spin-momentum locking responses. For example, the spin-momentum locking response has been observed in topological electromagnetic wave systems. The angular momentum of the wave function of the electric field constitutes the pseudospin²⁶. In thermal diffusion systems, temperature distributions in unit cells correspond to the electric fields of dipole and quadrupole orbitals. However, the physical quantity in diffusion systems corresponding to the magnetic field has not been identified. As the relationship between the wave and diffusion system has not yet been established, this is one of the future works.

Methods

Here, we show the parameters in the numerical simulations. The time evolution of the temperature is calculated by the MEMS module in COMSOL Multiphysics. We consider the finite structure consisting of 13×12 unit cells to obtain the edge states between the ordinary and topological unit cells, see Fig. 3a. Each unit cell has six disc-shaped sites with a thickness of 10 mm and a diameter of 20 mm. The cells have intra- and intercell connections using the beam of length $L = 15$ mm and width $w = 2$ mm and an effective thermal diffusivity D_1 (D_2) (see Fig. 1a). The effective thermal diffusivities are described as

$$D_{1(2)} = \frac{\lambda_{1(2)}}{c\rho L^2}, \quad (6)$$

where λ_1 (λ_2) is the thermal conductivity of the intra- and interbeam in the unit cell, and c and ρ are the heat capacity and mass density of a constitutional material, respectively. We assume that the structure consists of Aluminum, i.e., $c = 900 \text{ J kg}^{-1} \text{ K}^{-1}$ and $\rho = 2700 \text{ kg m}^{-3}$. We adjust $\lambda_{1(2)}$ to obtain the desired value of $D_{1(2)}$ in the simulations. Specifically, we set $\lambda_1 = 328.05$ (418.2638) $\text{W m}^{-1} \text{ K}^{-1}$ and $\lambda_2 = 464.7375$ (283.2165) $\text{W m}^{-1} \text{ K}^{-1}$ to be $D_1 = 0.6$ (0.765) and $D_2 = 0.85$ (0.518) in the topological (ordinary) state, respectively. The thermal conductivity of all sites is $238 \text{ W m}^{-1} \text{ K}^{-1}$. Note that by changing the beam length L instead of $\lambda_{1(2)}$, we will be able to tune $D_{1(2)}$ in future experimental demonstrations. For example, we would connect the sites with straight or meandering beams. We can indeed design the values of D_1 and D_2 of the topological (ordinary) state without changes in the intrinsic thermal conductivity of aluminum ($\lambda = 238 \text{ W m}^{-1} \text{ K}^{-1}$) when we set the intrabeam to $L = 12.776$ (11.315) mm and the interbeam to $L = 10.734$ (13.751) mm in the topological (ordinary) state, respectively.

We set the initial temperatures to each site of the unit cells to be the temperature distribution of the edge modes. The individual initial temperatures on each site are calculated from the eigenfunctions obtained from Eq. (1)-based eigen equation. We apply adiabatic boundaries on the entire surface of the structure to eliminate thermal radiation and convection. In the numerical model, we design the thermal diffusivities of the beams by directly

adjusting the value of thermal conductivity in the original material parameters. The temperature is calculated in the time duration from 0 to 100 s with the step of 2 s.

Data availability

The data that support the findings of this study can be provided from the corresponding author upon reasonable request.

Received: 16 April 2023; Accepted: 1 December 2023;

Published online: 20 December 2023

References

- Zhao, E. Topological circuits of inductors and capacitors. *Ann. Phys.* **399**, 289–313 (2018).
- Li, Y. et al. Topological lc-circuits based on microstrips and observation of electromagnetic modes with orbital angular momentum. *Nat. Commun.* **9**, 4598 (2018).
- Wang, Z., Chong, Y., Joannopoulos, J. D. & Soljacic, M. Observation of unidirectional backscattering-immune topological electromagnetic states. *Nature* **461**, 772–775 (2009).
- Hasan, M. Z. & Kane, C. L. Colloquium: topological insulators. *Rev. Mod. Phys.* **82**, 3045–3067 (2010).
- Qi, X.-L. & Zhang, S.-C. Topological insulators and superconductors. *Rev. Mod. Phys.* **83**, 1057–1110 (2011).
- Lee, C. H. et al. Topoelectrical circuits. *Commun. Phys.* **1**, 39 (2018).
- Darabi, A., Collet, M. & Leamy, M. J. Experimental realization of a reconfigurable electroacoustic topological insulator. *Proc. Natl Acad. Sci. USA* **117**, 16138–16142 (2020).
- Lee, T. & Iizuka, H. Bragg scattering based acoustic topological transition controlled by local resonance. *Phys. Rev. B* **99**, 064305 (2019).
- Zhang, X., Xiao, M., Cheng, Y., Lu, M.-H. & Christensen, J. Topological sound. *Commun. Phys.* **1**, 97 (2018).
- Liu, Y., Chen, X. & Xu, Y. Topological phononics: from fundamental models to real materials. *Adv. Funct. Mater.* **30**, 1904784 (2019).
- Yu, S. Y. et al. Elastic pseudospin transport for integrable topological phononic circuits. *Nat. Commun.* **9**, 3072 (2018).
- Cha, J., Kim, K. W. & Daraio, C. Experimental realization of on-chip topological nanoelectromechanical metamaterials. *Nature* **564**, 229–233 (2018).
- Vila, J., Pal, R. K. & Ruzzene, M. Observation of topological valley modes in an elastic hexagonal lattice. *Phys. Rev. B* **96**, 134307 (2017).
- Wang, W. et al. Robust fano resonance in a topological mechanical beam. *Phys. Rev. B* **101**, 024101 (2020).
- Matlack, K. H., Serra-Garcia, M., Palermo, A., Huber, S. D. & Daraio, C. Designing perturbative metamaterials from discrete models. *Nat. Mater.* **17**, 323–328 (2018).
- Funayama, K., Yatsugi, K., Miura, A. & Iizuka, H. Control of coupling between micromechanical topological waveguides. *Int. J. Mech. Sci.* **236**, 107755 (2022).
- Peng, Y., Bao, Y. & von Oppen, F. Boundary green functions of topological insulators and superconductors. *Phys. Rev. B* **95**, 235143 (2017).
- Su, W. P., Schrieffer, J. R. & Heeger, A. J. Solitons in polyacetylene. *Phys. Rev. Lett.* **42**, 1698–1701 (1979).
- Lan, C., Hu, G., Tang, L. & Yang, Y. Energy localization and topological protection of a locally resonant topological metamaterial for robust vibration energy harvesting. *J. Appl. Phys.* **129**, 184502 (2021).
- Lin, S., Zhang, L., Tian, T., Duan, C. K. & Du, J. Dynamic observation of topological soliton states in a programmable nanomechanical lattice. *Nano Lett.* **21**, 1025–1031 (2021).
- Engelhardt, G., Benito, M., Platero, G., Schaller, G. & Brandes, T. Random-walk topological transition revealed via electron counting. *Phys. Rev. B* **96**, 241404(R) (2017).
- Tian, T. et al. Experimental realization of nonreciprocal adiabatic transfer of phonons in a dynamically modulated nanomechanical topological insulator. *Phys. Rev. Lett.* **129**, 215901 (2022).
- Zangeneh-Nejad, F. & Fleury, R. Nonlinear second-order topological insulators. *Phys. Rev. Lett.* **123**, 053902 (2019).
- Fan, H., Xia, B., Tong, L., Zheng, S. & Yu, D. Elastic higher-order topological insulator with topologically protected corner states. *Phys. Rev. Lett.* **122**, 204301 (2019).
- Schindler, F. et al. Higher-order topological insulators. *Sci. Adv.* **4**, eaat0346 (2018).
- Wu, L.-H. & Hu, X. Scheme for achieving a topological photonic crystal by using dielectric material. *Phys. Rev. Lett.* **114**, 223901 (2015).
- Zhang, Z. et al. Topological creation of acoustic pseudospin multipoles in a flow-free symmetry-broken metamaterial lattice. *Phys. Rev. Lett.* **118**, 084303 (2017).
- Davis, R. J., Bisharat, D. J. & Sievenpiper, D. F. Classical-to-topological transmission line couplers. *Appl. Phys. Lett.* **118**, 131102 (2021).
- Yu, Z., Ren, Z. & Lee, J. Phononic topological insulators based on six-petal holey silicon structures. *Sci. Rep.* **9**, 1805 (2019).
- Hu, H. et al. Observation of topological edge states in thermal diffusion. *Adv. Mater.* **34**, e2202257 (2022).
- Qi, M. et al. Geometric phase and localized heat diffusion. *Adv. Mater.* **32**, e2202241 (2022).
- Yoshida, T. & Hatsugai, Y. Bulk-edge correspondence of classical diffusion phenomena. *Sci. Rep.* **11**, 888 (2021).
- Xu, G. et al. Diffusive topological transport in spatiotemporal thermal lattices. *Nat. Phys.* **18**, 450–456 (2022).
- Wu, H. et al. Higher-order topological states in thermal diffusion. *Adv. Mater.* **35**, 2210825 (2023).
- Fukui, T., Yoshida, T. & Hatsugai, Y. Higher-order topological heat conduction on a lattice for detection of corner states. *Phys. Rev. E* **108**, 024112 (2023).
- Weidemann, S. et al. Topological funneling of light. *Science* **368**, 311–314 (2020).
- Zhang, X., Tian, Y., Jiang, J.-H., Lu, M.-H. & Chen, Y.-F. Observation of higher-order non-hermitian skin effect. *Nat. Commun.* **12**, 5377 (2021).
- Xu, G., Zhou, X., Yang, S., Wu, J. & Qiu, C.-W. Observation of bulk quadrupole in topological heat transport. *Nat. Commun.* **14**, 3252 (2023).

Author contributions

All authors contributed extensively to the work presented in this paper. H.T. managed this project. K.F. and H.T. carried out the theoretical analysis with the assistance of A.M. and J.H. K.F. designed and calculated the numerical model.

Competing interests

The authors declare no competing interests.

Additional information

Supplementary information The online version contains supplementary material available at <https://doi.org/10.1038/s42005-023-01490-9>.

Correspondence and requests for materials should be addressed to Keita Funayama.

Peer review information *Communications Physics* thanks the anonymous reviewers for their contribution to the peer review of this work. A peer review file is available.

Reprints and permission information is available at <http://www.nature.com/reprints>

Publisher's note Springer Nature remains neutral with regard to jurisdictional claims in published maps and institutional affiliations.



Open Access This article is licensed under a Creative Commons Attribution 4.0 International License, which permits use, sharing, adaptation, distribution and reproduction in any medium or format, as long as you give appropriate credit to the original author(s) and the source, provide a link to the Creative Commons license, and indicate if changes were made. The images or other third party material in this article are included in the article's Creative Commons license, unless indicated otherwise in a credit line to the material. If material is not included in the article's Creative Commons license and your intended use is not permitted by statutory regulation or exceeds the permitted use, you will need to obtain permission directly from the copyright holder. To view a copy of this license, visit <http://creativecommons.org/licenses/by/4.0/>.

© The Author(s) 2023